ACS APPLIED MATERIALS & INTERFACES

www.acsami.org Research Article

Tuning of Optical Phonons in α-MoO_3–VO_2 Multilayers

Sina Abedini Dereshgi, Maria Cristina Larciprete, Marco Centini, Akshay A. Murthy, Kechao Tang, Junqiao Wu, Vinayak P. Dravid, and Koray Aydin*

Cite This: *ACS Appl. Mater. Interfaces* 2021, 13, 48981–48987 Read Online

ACCESS | Metrics & More | Article Recommendations | Supporting Information

ABSTRACT: Merging the properties of VO_2 and van der Waals (vdW) materials has given rise to novel tunable photonic devices. Despite recent studies on the effect of the phase change of VO_2 on tuning near-field optical response of phonon polaritons in the infrared range, active tuning of optical phonons (OPhs) using far-field techniques has been scarce. Here, we investigate the tunability of OPhs of α-MoO_3 in a multilayer structure with VO_2. Our experiments show the frequency and intensity tuning of 2 cm^{-1} and 11% for OPhs in the [100] direction and 2 cm^{-1} and 28% for OPhs in the [010] crystal direction of α-MoO_3. Using the effective medium theory and dielectric models of each layer, we verify these findings with simulations. We then use loss tangent analysis and remove the effect of the substrate to understand the origin of these spectral characteristics. We expect that these findings will assist in intelligently designing tunable photonic devices for infrared applications, such as tunable camouflage and radiative cooling devices.

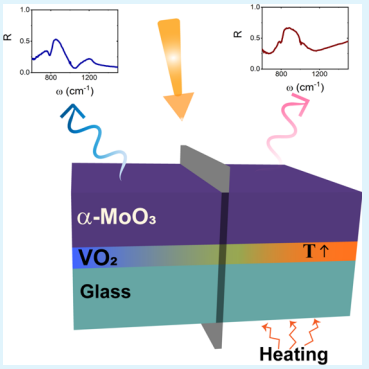

KEYWORDS: *optical phonons, vdW materials, phase-change materials, Fabry–Perot cavity, active tuning*

INTRODUCTION

Layered van der Waals (vdW) materials have revolutionized the photonic devices with their ease of integration in forming heterostructures[1] and their intriguing characteristics that have triggered novel applications. Specifically, the naturally occurring hyperbolicity of vdW materials such as hexagonal boron nitride (hBN) and α-MoO_3 has led to the prediction and demonstration of canalization,[2] sub-wavelength imaging,[3] negative refraction,[4] photonic magic angle,[5−7] and high infrared absorption.[8] The inherent layered nature of these vdW materials is quite valuable in integrating with other materials to create structures whose optical and electrical responses can be tuned dynamically.

Phase-change materials have proven to be an indispensable tool in the area of optical modulation, offering repeatable and active modulation. Since the first revelation of its dynamic phase-change properties in 1959,[9] the interest in the active modulation properties of VO_2 has been thriving. When the temperature applied to VO_2 increases beyond a critical point (T_c), insulator-to-metal transition (IMT) takes place, which renders its monoclinic (insulator) phase rutile (metallic).[10] While the microscopic dynamics of this intriguing phase transition for VO_2 remains elusive,[11] the experimental implementation of it in devices has been successful in the recent decade. The lower T_c required for the IMT of VO_2 than that of other phase-change materials,[9,12] along with a variety of possible routes to achieve IMT (thermally,[13] electrically,[14] mechanically,[15] and optically[16,17]), has provided ample opportunities to tailor the IMT of VO_2 to numerous applications.[18,19] The essence of optical modulation in the mentioned photonic applications is the IMT of VO_2, which marks a sizeable change in the refractive index of this material. Some of the notable applications include optical diodes,[20] tunable metamaterials,[21−23] thermal emitters,[10,24] and infrared absorbers.[25]

Marrying the tunability of VO_2 and the rich optical response of vdW materials through intricate designs, researchers have successfully demonstrated devices with tunable optical responses.[26,27] In near-field optics, α-MoO_3 and hBN are known to support hyperbolic phonon polaritons that yield increased photonic density of states and are highly sensitive to the optical characteristics of the immediate environment. This very fact has led to the realization of tunable hyperbolic phonon polaritons in both intensity and frequency through scattering-type scanning near-field optical microscopy characterization.[28,29] However, reports on the far-field tunability of the optical response of hyperbolic materials with VO_2 do not exist to the best of our knowledge. Unlike phonon polaritons which require momentum-matching techniques, the lattice vibration modes known as optical phonons (OPhs) can directly be coupled to photons.[30] α-MoO_3 is an outstanding example of a vdW material that has three Reststrahlen (RS) bands in the infrared region and demonstrates in-plane

Received: June 30, 2021
Accepted: September 21, 2021
Published: October 6, 2021

https://doi.org/10.1021/acsami.1c12320
ACS Appl. Mater. Interfaces 2021, 13, 48981–48987

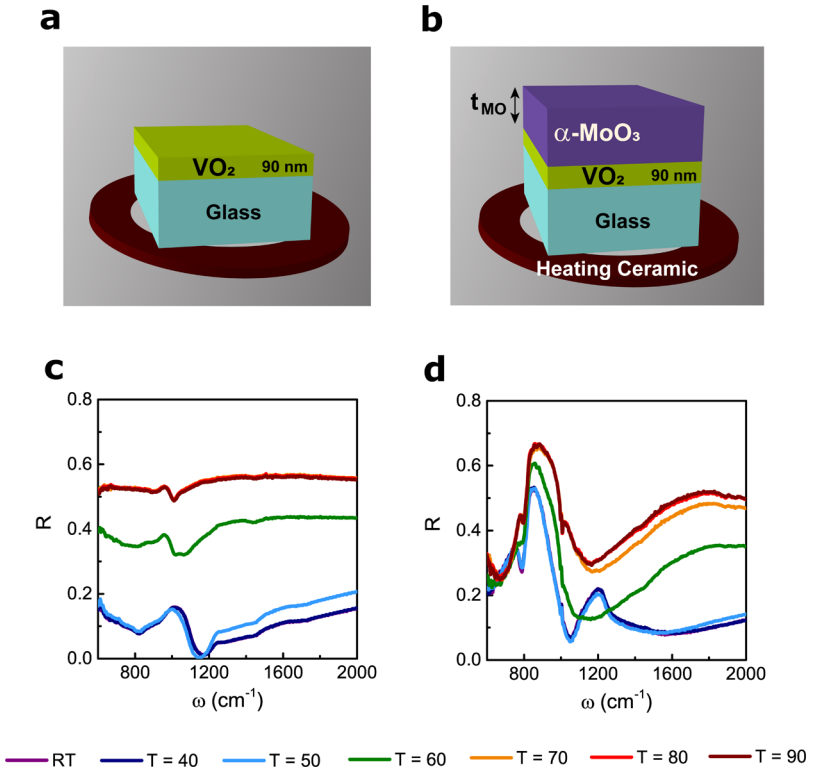

Figure 1. Schematic illustration of samples under study (a) without and (b) with the α-MoO_3 flake. Measured spectral reflectance with steps of 10 °C for samples (c) and (d) with the α-MoO_3 flake.

anisotropy from ultraviolet to infrared regions with three orthogonal OPh modes in the infrared region near respective transverse optical (TO) frequencies.[31−36] Benefitting the in-plane anisotropy of α-MoO_3 through OPhs can be consequential for polarization-sensitive photonic devices in the second infrared atmospheric window (8−14 μm, equivalent to 700−1400 cm^{-1}).[30,37] Another untapped potential of α-MoO_3 is its high reflectance in this atmospheric window, which can be consequential for radiative cooling and thermal camouflage applications,[38,39] which have been revitalized thanks to thin films[40] and metamaterials[39] research.[41,42] Camouflage requires high reflectance within the transmissive window.[39,43] The signature of the RS band is its high reflectivity; the RS bands in [100] and [010] directions of α-MoO_3 lie within this atmospheric window, which can make this material highly suitable for camouflage applications. The combination of α-MoO_3 and VO_2 can also pave the way to scalable tunable thermal camouflage applications.[43,44]

Here, we experimentally demonstrate the tunability of OPhs and cavity modes in α-MoO_3 with the IMT of VO_2 through far-field Fourier transform infrared (FTIR) measurements in a multilayer structure. From the experimental results, we find that the frequency and intensity of the reflected signal can be modulated. Our simulated results shed light on the origin of this spectral behavior. We finally conclude by demonstrating the inherent tunability in the OPh frequency and absorption intensity in α-MoO_3 that is possible through this type of heterostructure, which can pave the way for tunable, large-scale optical components for infrared applications.

RESULTS AND DISCUSSION

Design and Experiments. The structure investigated in this study is a multilayer system composed of a 90 nm VO_2 film on a SiO_2 substrate (Figure 1a) and an α-MoO_3 flake which is transferred onto VO_2−SiO_2 (Figure 1b). The temperature-dependent reflectance measurements are carried out using the FTIR system where the sample is placed onto a heating ceramic, as illustrated in Figure 1a,b. The measured spectral reflectance curves for different temperature values are depicted in Figure 1c,d for samples without (Figure 1a) and with the α-MoO_3 flake (Figure 1b), respectively.

As the temperature is increased in steps of 10 °C (Figure 1c,d), the IMT takes place, and the reflectance increases due to the metallic nature of VO_2 after the IMT. This dramatic change in spectral reflectance occurs around 70 °C, which corresponds to the VO_2 phase transformation being triggered.[11] From the reflectance curves for the sample with α-MoO_3 (Figure 1d), we observe a shift in the reflectance intensity for OPhs in the [100] direction (OPh_x) at 812 cm^{-1}.[30] Also evident from Figure 1d is a larger dip in reflectance for the room-temperature (RT) curve at 789 cm^{-1}, which corresponds to the Fabry−Perot (FP) mode due to the thick α-MoO_3 layer (air−MoO_3−VO_2 stack) which dissipates in the VO_2 layer. This mode blue-shifts (moves to a higher frequency) as the temperature increases due to the modified phase shift imparted on the reflected light off of the MoO_3−VO_2 interface. There is a small dip at 1008 cm^{-1}, evident in Figure 1d, which is due to the OPhs in the [010] direction of α-MoO_3 (OPh_z). For ω < 1000 cm^{-1}, the reflectance dips are attributed to the OPhs of SiO_2. The modes are modeled and discussed in further detail in the following section.

DISCUSSION

In order to investigate the impact of the phase change on OPhs of α-MoO_3, we first studied VO_2 in isolation. The spectral reflectance for the glass−VO_2 system (Figure 1a) is

https://doi.org/10.1021/acsami.1c12320
ACS Appl. Mater. Interfaces 2021, 13, 48981−48987

represented in Figure 1c. The IMT process for VO_2 starts with metallic islands that expand as temperature is increased, which can be modeled with the effective medium theory (EMT)[45,46]

$$\varepsilon_{\text{eff},j} = \varepsilon_{\text{I}} + \text{FF}\frac{\varepsilon_{\text{I}}(\varepsilon_{\text{M}} - \varepsilon_{\text{I}})}{\varepsilon_{\text{I}} + (1 - \text{FF})L_j(\varepsilon_{\text{M}} - \varepsilon_{\text{I}})}$$

where $\varepsilon_{\text{eff},j}$ is the effective dielectric function in direction j. ε_{I} and ε_{M} stand for, respectively, the insulator and metal phases of VO_2 taken from Wan et al.[47] (Supporting Information). The filling factor (FF) is the in-plane filling ratio of the metallic islands to the insulator host within the VO_2 film, which approaches 1 as the temperature is increased. L_j is the depolarization factor in direction j, which represents the shape of the metallic inclusion and satisfies $L_x + L_y + L_z = 1$.[48] Given the in-plane (transverse) isotropy of VO_2, the EMT yields in-plane and out-of-plane permittivities ($\varepsilon_x = \varepsilon_y \neq \varepsilon_z$). Since the heating is applied in steps of 10 °C with long wait times (slow heating steps), the inclusions are disk-like in shape, with the disk axis parallel to the optical axis (z direction). This translates to $L_x = L_y \approx 0$ and $L_z \approx 1$.[46] The Lorentz formulation is used for the SiO_2 model (Supporting Information), and a value of FF = 0.5 is used for the curves corresponding to 60 °C. α-MoO_3 is modeled with the Lorentz equation[34] (Supporting Information). The mentioned dielectric models are employed to a 4 × 4 transfer matrix method (TMM)[49] to simulate the reflectance curves for three distinct temperature values, that is, RT, 60 °C, and 90 °C. The simulation results for the sample without the α-MoO_3 layer are depicted in Figure 2a (dashed curves), which agree well with their corresponding measurement results (solid curves). The incident polarization angle is 30° for all measurements and simulations. The weighted-average incidence angle of the FTIR spectrum is 15°, which is also used for simulations.

The reflectance simulations for the structure with α-MoO_3 are compared to the measurements in Figure 2b, and Figure 2c illustrates a close-up view of the FP and OPh_x modes. As temperature rises from RT to 90 °C (hot), the measured FP mode demonstrates a frequency shift of 4 cm^{-1} from 789 to 794 cm^{-1} and an intensity change of 0.15 from 0.27 to 0.42. The simulated values suggest a similar shift of 7 cm^{-1} in frequency and 0.26 in intensity. The measured OPh_x mode at 812 cm^{-1} demonstrates an intensity shift of 0.11 and a frequency shift of 2 cm^{-1}. Although the simulations show a frequency shift of 0.94 cm^{-1} for the OPh_x mode, such a small shift is too close to the highest resolution of our FTIR system, which is 2 cm^{-1}, which can explain the higher shift observed in measurements. Small frequency shifts are also expected in the literature for thin layers.[50] The OPh_z mode (997 cm^{-1}) in Figure 2d demonstrates a frequency shift of 2 cm^{-1} and an intensity shift of 0.28 when the temperature increases from RT to hot. The simulations suggest a frequency shift of 1.2 cm^{-1}.

The reflectance value for the RT phase remains high for the transmissive window (700−1250 cm^{-1}) and is low for the nontransmissive window (1250−2000 cm^{-1}), demonstrating camouflage characteristics. Once VO_2 changes the phase to hot, aside from the increased reflectance (better camouflage capability), the absorption is also increased (Supporting Information) within the nontransmissive window (1250−2000 cm^{-1}). Hence, the emissivity increases within this band, and radiative cooling is achieved in the hot phase.

The highest observed frequency shift is for the FP (or the Etalon) mode trapped inside α-MoO_3 and dissipated to VO_2. The average thickness of the measurement area for the α-MoO_3 layer is 1.27 μm (Supporting Information). Figure 3 demonstrates the spectral reflectance for different α-MoO_3 thicknesses (t_{MO}) for RT and hot phases of VO_2. The blue traces in Figure 3a (RT) starting near 800 cm^{-1} to smaller frequency values are the FP modes in α-MoO_3. As the thickness increases, more FP modes are realizable in α-MoO_3. A similar scenario is observed in the hot simulation results of Figure 3b. The sharp vertical blue lines near 1000 cm^{-1} in Figure 3a,b are OPh_z modes. The red regions between 800 and 1000 cm^{-1} in Figure 3a,b are high-reflectance bands representing the RS bands in the [100] direction of α-MoO_3, a signature of the natural hyperbolicity of this material. As temperature is increased, the reflectance increases in general due to the IMT of VO_2. The behavior of reflectance and transmittance can be explained by investigating absorption. The lossy behavior of α-MoO_3 is overshadowed by VO_2 for ω > 1000 cm^{-1} and ω < 800 cm^{-1} (Supporting Information). As temperature increases, the VO_2 layer becomes more lossy.[15] For 800 cm^{-1} < ω < 1000 cm^{-1}, the RS band in the [100] direction of α-MoO_3 reflects the incident light, and the light does not reach VO_2 underneath to be dissipated. An insightful and simple definition to understand the dominance of the absorption behavior of VO_2 is the electric loss tangent.[51,52] The absolute inverse electric loss tangent is defined as $\tan^{-1}\delta_e = |\varepsilon_1|/\varepsilon_2$, where ε_1 and ε_2 are, respectively, the real and imaginary parts of the permittivity. A lower inverse tangent signifies higher absorption, which is the case for VO_2. For ω < 800 cm^{-1}, for example, VO_2 is the most lossy material in the multilayer system (Supporting Information).

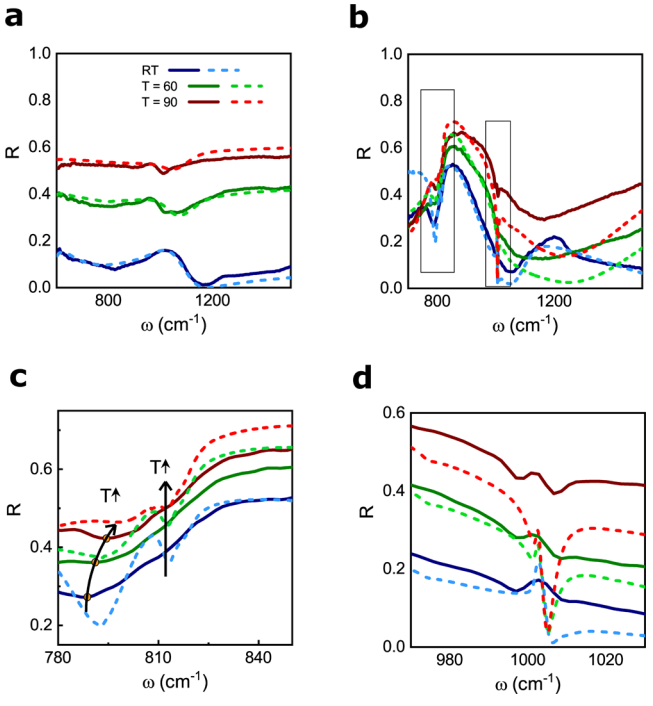

Figure 2. Simulated (dashed) and measured (solid) spectral reflectance for the sample (a) without and (b) with the α-MoO_3 flake. Zoomed-in selections from (b) near (c) 800 cm^{-1}, representing OPh_x and FP modes, and (d) 1000 cm^{-1}, representing OPh_z and SiO_2 substrate phonon modes. The zoomed-in selections are represented by rectangles with black solid lines in (b). The arrows in (c) demonstrate the change of resonances (FP and OPh_x) as the applied temperature is increased.

https://doi.org/10.1021/acsami.1c12320
ACS Appl. Mater. Interfaces 2021, 13, 48981−48987

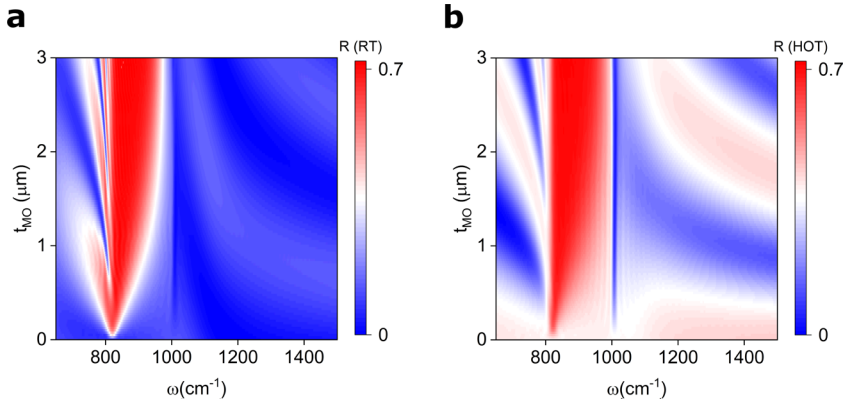

Figure 3. Spectral reflectance vs α-MoO_3 thickness (t_{MO}) for the sample depicted in Figure 1b at (a) FF = 0 (RT) and (b) FF = 1 (hot).

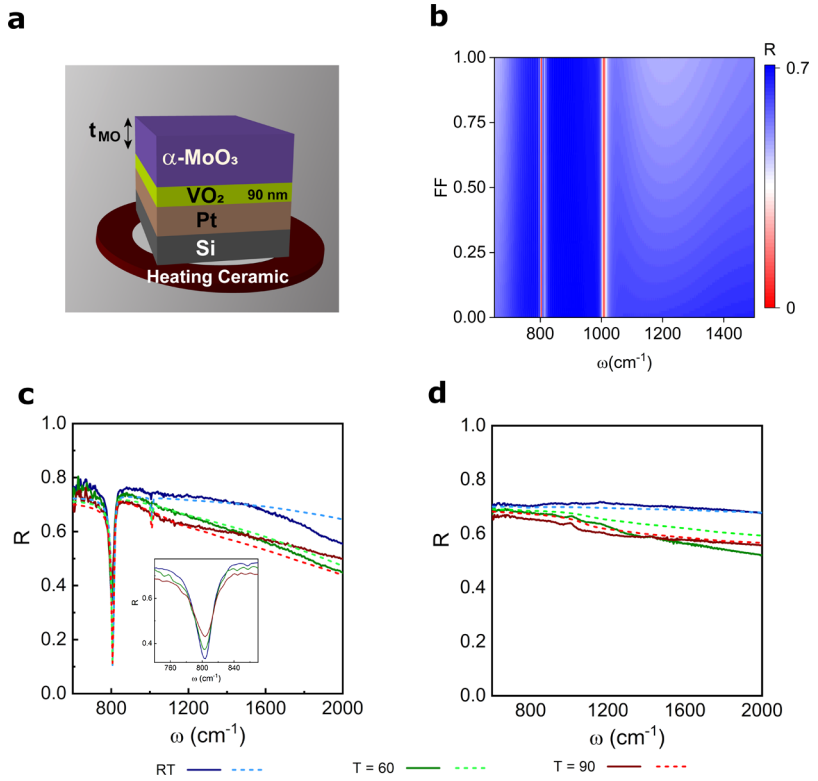

Figure 4. (a) Schematic illustration of the sample under investigation and (b) spectral reflectance of this sample vs FF. The simulated (dashed) and measured (solid) spectral reflectance of the sample in (a) for three applied temperature values, (c) with and (d) without the α-MoO_3 flake on the top. The inset of (c) is a close-up view of the measured OPh_x resonance mode.

To further verify the observed modes and shifts, another sample is fabricated with layers consisting of Pt (100 nm), VO_2 (90 nm), and α-MoO_3 from the bottom to the top, as illustrated in Figure 4a. This structure includes a 220 nm α-MoO_3 layer (Supporting Information). Using Pt as a bottom reflector layer isolates the observed reflectance from the effects of glass phonon modes near 997 cm^{-1}. Figure 4b demonstrates the simulated spectral reflectance versus FF (which is temperature-dependent) plot that clearly outlines the observed OPh_x and OPh_z modes, respectively, near 810 and 1006 cm^{-1}. Due to the thinner α-MoO_3 layer in this sample, FP modes do not exist. Figure 4c,d demonstrates the measured (solid) and simulated (dotted) spectral reflectance at three different temperature values. The experimental OPh_x mode (dip) in Figure 4c demonstrates a blue shift of 2 cm^{-1} and an intensity shift of 0.1 as temperature is increased to hot from RT (inset of Figure 4c). Simulated shifts are 0.53 and 0.08 cm^{-1}. Figure 4d demonstrates the measured and simulated spectral reflectance curves for the same sample without α-MoO_3, which agree well. The difference between the simulation and measurement mainly arises for the intensity of the resonances, which is expected due to the sharpness of these resonances and the limiting resolution of FTIR spectra. Throughout this study, the chosen thickness values for α-MoO_3 and VO_2 were not the optimum case and were chosen as the reported values due to the fabrication and transfer challenges that are concomitant to current VO_2 and α-MoO_3 growth techniques. The frequency and intensity tuning can be further enhanced by modifying the thicknesses of the layers (Supporting Information).

https://doi.org/10.1021/acsami.1c12320
ACS Appl. Mater. Interfaces 2021, 13, 48981−48987

CONCLUSIONS

We demonstrated experimentally a frequency tuning of 2 cm^{-1} for both OPh_x and OPh_z modes in [100] and [010] crystal directions of α-MoO_3. We reported the reflectance intensity tuning of 11% and 0.28 for these phonon modes. Using the EMT and dielectric models of each layer along with the TMM and finite-difference time-domain simulations, the measurements were verified with simulations. The origin of observed and simulated spectral characteristics was also traced back using loss tangent analysis. The effect of the glass substrate was eliminated using a Pt metal layer instead, which further verified the shifts and modes. Our findings can be tailored to the design of advanced tunable photonic devices in the second atmospheric window in the infrared region.

METHODS

VO_2 Deposition. The VO_2 thin films were deposited in a 5 mTorr O_2 environment at 550 °C substrate temperature, and the PLD laser energy was set to be 321 mJ with 5 Hz pulse frequency. A postdeposition annealing at 550 °C for 30 min was performed in the same 5 mTorr O_2 environment. This temperature is safe for the thick Pt layer and does not allow for the dewetting of the underlying Pt layer.[53] The follow-up step does not introduce thermal shock to the sample since the flakes are grown and transferred.

α-MoO_3 Deposition and Transfer. α-MoO_3 flakes were grown using low-pressure physical vapor deposition. For this process, 50 mg of MoO_3 (Sigma-Aldrich) powder was spread evenly within an alumina boat. This boat was placed within a 1 inch diameter quartz tube and at the center of a small Lindberg tube furnace. A 41 $in.^2$ rectangular piece of a SiO_2/Si wafer (300 nm oxide thickness) was placed face-up downstream in a colder zone of the furnace. These pieces were suspended on the top of the alumina boat and were located roughly 4 cm from the center region. The pressure was maintained at 2.8 Torr with a carrier gas of O_2 at a flow rate of 25 sccm. The center of the furnace was then heated to 675 °C over a period of 25 min and then to 700 °C over a period of 5 min. Upon reaching 700 °C, the furnace was immediately opened, thereby quenching the deposition. A simple tape transfer was adopted to deposit the flakes onto VO_2 films.

FTIR Characterization. Mid-infrared reflectance measurements were obtained with a Hyperion 2000 IR microscope coupled to a Bruker Vertex 70 FTIR spectrometer. For the FP structures, a mercury cadmium telluride detector was used. The Cassegrain objective was 15×, and the aperture dimensions were 30 × 30 μm^2.

ASSOCIATED CONTENT

Supporting Information

The Supporting Information is available free of charge at https://pubs.acs.org/doi/10.1021/acsami.1c12320.

Dielectric model of the layers, scanning electron microscopy of the α-MoO_3 flakes and their surface profiles, simulation of the effect of heating on the transient optical response of the devices, and loss tangent analysis for the devices (PDF)

AUTHOR INFORMATION

Corresponding Author

Koray Aydin − *Department of Electrical and Computer Engineering, Northwestern University, Evanston, Illinois 60208, United States;* orcid.org/0000-0002-3268-2216; Email: aydin@northwestern.edu

Authors

Sina Abedini Dereshgi − *Department of Electrical and Computer Engineering, Northwestern University, Evanston, Illinois 60208, United States;* orcid.org/0000-0003-2929-0817

Maria Cristina Larciprete − *Dipartimento di Scienze di Base ed Applicate per l'Ingegneria, Sapienza Università di Roma, 00161 Rome, Italy*

Marco Centini − *Dipartimento di Scienze di Base ed Applicate per l'Ingegneria, Sapienza Università di Roma, 00161 Rome, Italy*

Akshay A. Murthy − *Department of Materials Science and Engineering and International Institute for Nanotechnology, Northwestern University, Evanston, Illinois 60208, United States;* orcid.org/0000-0001-7677-6866

Kechao Tang − *Department of Materials Science and Engineering, University of California, Berkeley, California 94720, United States*

Junqiao Wu − *Department of Materials Science and Engineering, University of California, Berkeley, California 94720, United States; Materials Sciences Division, Lawrence Berkeley National Laboratory, Berkeley, California 94720, United States;* orcid.org/0000-0002-1498-0148

Vinayak P. Dravid − *Department of Materials Science and Engineering, International Institute for Nanotechnology, and Northwestern University Atomic and Nanoscale Characterization Experimental Center (NUANCE), Northwestern University, Evanston, Illinois 60208, United States;* orcid.org/0000-0002-6007-3063

Complete contact information is available at: https://pubs.acs.org/10.1021/acsami.1c12320

Author Contributions

S.A.D. was involved in the design, simulations, measurements, and writing of the manuscript. M.C.L. and M.C. contributed to the simulation and modeling of the system. A.A.M. contributed to the growth of α-MoO_3 flakes and their transfer. K.T. was involved in the deposition of VO_2 films. All authors read and commented on the manuscript, and J.W., V.P.D., and K.A. supervised the project.

Notes

The authors declare no competing financial interest.

ACKNOWLEDGMENTS

K.A. acknowledges the support from the Office of Naval Research Young Investigator Program (ONR-YIP) award (N00014-17-1-2425). The program manager is Brian Bennett. K.A. and V.P.D. acknowledge partial support from the Air Force Office of Scientific Research under award number FA9550-17-1-0348. This material is partially supported by the National Science Foundation under grant no. DMR-1929356. K.A. and M.L. also acknowledge the support from the University La Sapienza for the Visiting Professor Program 2018 (Bando Professori Visitatori 2018) as well as for the Sapienza Research Program 2017 (Progetti di Ateneo 2017). The material preparation was supported by the National Science Foundation under grant no. ECCS-1953803. A.A.M. gratefully acknowledges support from the Ryan Fellowship and the International Institute for Nanotechnology (IIN) at Northwestern University. This work made use of the EPIC, Keck-II, SPID, and Northwestern University Micro/Nano Fabrication Facility (NUFAB) facilities of Northwestern University's NUANCE Center, which has received support from the Soft and Hybrid Nanotechnology Experimental (SHyNE) Resource (NSF ECCS-1542205); the MRSEC

program (NSF DMR-1720319) at the Materials Research Center; the IIN; the Keck Foundation; and the State of Illinois, through the IIN.

ABBREVIATIONS

α-MoO_3, α-phase molybdenum trioxide
h-BN, hexagonal boron nitride
FP, Fabry−Perot
IMT, insulator-to-metal transition
EMT, effective medium theory
FF, filling factor
OPh, optical phonon
TO, transverse optical
LO, longitudinal optical
RS band, Reststrahlen band
vdW, van der Waals
s-SNOM, scattering-type scanning near-field optical microscopy
FDTD, finite-difference time-domain
FTIR, Fourier transform infrared

REFERENCES

(1) Grigorenko, A. N.; Polini, M.; Novoselov, K. S. Graphene Plasmonics. *Nat. Photonics* **2012**, *6*, 749−758.
(2) Correas-Serrano, D.; Alù, A.; Gomez-Diaz, J. S. Plasmon Canalization and Tunneling over Anisotropic Metasurfaces. *Phys. Rev. B: Condens. Matter Mater. Phys.* **2017**, *96*, 075436.
(3) Li, P.; Lewin, M.; Kretinin, A. V.; Caldwell, J. D.; Novoselov, K. S.; Taniguchi, T.; Watanabe, K.; Gaussmann, F.; Taubner, T. Hyperbolic Phonon-Polaritons in Boron Nitride for Near-Field Optical Imaging and Focusing. *Nat. Commun.* **2015**, *6*, 7507.
(4) Lin, X.; Yang, Y.; Rivera, N.; López, J. J.; Shen, Y.; Kaminer, I.; Chen, H.; Zhang, B.; Joannopoulos, J. D.; Soljačić, M. All-Angle Negative Refraction of Highly Squeezed Plasmon and Phonon Polaritons in Graphene−Boron Nitride Heterostructures. *Proc. Natl. Acad. Sci. U.S.A.* **2017**, *114*, 6717−6721.
(5) Hu, G.; Ou, Q.; Si, G.; Wu, Y.; Wu, J.; Dai, Z.; Krasnok, A.; Mazor, Y.; Zhang, Q.; Bao, Q.; Qiu, C.-W.; Alù, A. Topological Polaritons and Photonic Magic Angles in Twisted α-MoO_3 Bilayers. *Nature* **2020**, *582*, 209−213.
(6) Chen, M.; Lin, X.; Dinh, T. H.; Zheng, Z.; Shen, J.; Ma, Q.; Chen, H.; Jarillo-Herrero, P.; Dai, S. Configurable Phonon Polaritons in Twisted α-MoO_3. *Nat. Mater.* **2020**, *19*, 1307−1311.
(7) Duan, J.; Capote-Robayna, N.; Taboada-Gutiérrez, J.; Álvarez-Pérez, G.; Prieto, I.; Martín-Sánchez, J.; Nikitin, A. Y.; Alonso-González, P. Twisted Nano-Optics: Manipulating Light at the Nanoscale with Twisted Phonon Polaritonic Slabs. *Nano Lett.* **2020**, *20*, 5323−5329.
(8) Song, X.; Dereshgi, S. A.; Palacios, E.; Xiang, Y.; Aydin, K. Enhanced Interaction of Optical Phonons in h-BN with Plasmonic Lattice and Cavity Modes. *ACS Appl. Mater. Interfaces* **2021**, *13*, 25224−25233.
(9) Morin, F. J. Oxides Which Show a Metal-to-Insulator Transition at the Neel Temperature. *Phys. Rev. Lett.* **1959**, *3*, 34.
(10) Larciprete, M. C.; Centini, M.; Paoloni, S.; Abedini Dereshgi, S.; Tang, K.; Wu, J.; Aydin, K. Adaptive Tuning of Infrared Emission Using VO_2 Thin Films. *Sci. Rep.* **2020**, *10*, 11544.
(11) Cueff, S.; John, J.; Zhang, Z.; Parra, J.; Sun, J.; Orobtchouk, R.; Ramanathan, S.; Sanchis, P. VO_2 Nanophotonics. *APL Photonics* **2020**, *5*, 110901.
(12) Liu, H.; Lu, J.; Wang, X. R. Metamaterials Based on the Phase Transition of VO_2. *Nanotechnol* **2017**, *29*, 024002.
(13) Nag, J.; Haglund, R. F., Jr.; Andrew Payzant, E.; More, K. L. Non-Congruence of Thermally Driven Structural and Electronic Transitions in VO_2. *J. Appl. Phys.* **2012**, *112*, 103532.
(14) Ko, C.; Ramanathan, S. Observation of Electric Field-Assisted Phase Transition in Thin Film Vanadium Oxide in a Metal-Oxide-Semiconductor Device Geometry. *Appl. Phys. Lett.* **2008**, *93*, 252101.
(15) Aetukuri, N. B.; Gray, A. X.; Drouard, M.; Cossale, M.; Gao, L.; Reid, A. H.; Kukreja, R.; Ohldag, H.; Jenkins, C. A.; Arenholz, E.; Roche, K. P.; Dürr, H. A.; Samant, M. G.; Parkin, S. S. P. Control of the Metal−Insulator Transition in Vanadium Dioxide by Modifying Orbital Occupancy. *Nat. Phys.* **2013**, *9*, 661−666.
(16) Cavalleri, A.; Dekorsy, T.; Chong, H. H. W.; Kieffer, J. C.; Schoenlein, R. W. Evidence for a Structurally-Driven Insulator-to-Metal Transition in VO_2: A View From the Ultrafast Timescale. *Phys. Rev. B: Condens. Matter Mater. Phys.* **2004**, *70*, 161102.
(17) Lei, D. Y.; Appavoo, K.; Ligmajer, F.; Sonnefraud, Y.; Haglund, R. F., Jr.; Maier, S. A. Optically-Triggered Nanoscale Memory Effect in a Hybrid Plasmonic-Phase Changing Nanostructure. *ACS Photonics* **2015**, *2*, 1306−1313.
(18) Khan, Z.; Singh, P.; Ansari, S. A.; Manippady, S. R.; Jaiswal, A.; Saxena, M. VO_2 Nanostructures for Batteries and Supercapacitors: A Review. *Small* **2021**, *17*, 2006651.
(19) Long, L.; Taylor, S.; Wang, L. Enhanced Infrared Emission by Thermally Switching the Excitation of Magnetic Polariton with Scalable Microstructured VO_2 Metasurfaces. *ACS Photonics* **2020**, *7*, 2219−2227.
(20) Wan, C.; Horak, E. H.; King, J.; Salman, J.; Zhang, Z.; Zhou, Y.; Roney, P.; Gundlach, B.; Ramanathan, S.; Goldsmith, R. H.; Kats, M. A. Limiting Optical Diodes Enabled by the Phase Transition of Vanadium Dioxide. *ACS Photonics* **2018**, *5*, 2688−2692.
(21) Wuttig, M.; Bhaskaran, H.; Taubner, T. Phase-Change Materials for Non-Volatile Photonic Applications. *Nat. Photonics* **2017**, *11*, 465−476.
(22) Ligmajer, F.; Kejík, L.; Tiwari, U.; Qiu, M.; Nag, J.; Konečný, M.; Šikola, T.; Jin, W.; Haglund, R. F., Jr.; Appavoo, K.; Lei, D. Y. Epitaxial VO_2 Nanostructures: A Route to Large-Scale, Switchable Dielectric Metasurfaces. *ACS Photonics* **2018**, *5*, 2561−2567.
(23) Kocer, H.; Butun, S.; Banar, B.; Wang, K.; Tongay, S.; Wu, J.; Aydin, K. Thermal Tuning of Infrared Resonant Absorbers Based on Hybrid Gold-VO_2 Nanostructures. *Appl. Phys. Lett.* **2015**, *106*, 161104.
(24) Kats, M. A.; Blanchard, R.; Zhang, S.; Genevet, P.; Ko, C.; Ramanathan, S.; Capasso, F. Vanadium Dioxide as a Natural Disordered Metamaterial: Perfect Thermal Emission and Large Broadband Negative Differential Thermal Emittance. *Phys. Rev. X* **2013**, *3*, 041004.
(25) Liu, Z.; Banar, B.; Butun, S.; Kocer, H.; Wang, K.; Scheuer, J.; Wu, J.; Aydin, K. Dynamic Infrared Thin-Film Absorbers with Tunable Absorption Level Based on VO_2 Phase Transition. *Opt. Mater. Express* **2018**, *8*, 2151−2158.
(26) Song, X.; Liu, Z.; Scheuer, J.; Xiang, Y.; Aydin, K. Tunable Polaritonic Metasurface Absorbers in Mid-IR Based on Hexagonal Boron Nitride and Vanadium Dioxide Layers. *J. Phys. D Appl. Phys.* **2019**, *52*, 164002.
(27) Hajian, H.; Ghobadi, A.; Serebryannikov, A. E.; Butun, B.; Vandenbosch, G. A. E.; Ozbay, E. VO_2-hBN-Graphene-Based Bi-Functional Metamaterial for Mid-Infrared Bi-Tunable Asymmetric Transmission and Nearly Perfect Resonant Absorption. *J. Opt. Soc. Am. B* **2019**, *36*, 1607−1615.
(28) Dai, S.; Zhang, J.; Ma, Q.; Kittiwatanakul, S.; McLeod, A.; Chen, X.; Corder, S. G.; Watanabe, K.; Taniguchi, T.; Lu, J.; Dai, Q.; Jarillo-Herrero, P.; Liu, M.; Basov, D. N. Phase-Change Hyperbolic Heterostructures for Nanopolaritonics: A Case Study of hBN/VO_2. *Adv. Mater.* **2019**, *31*, 1900251.
(29) Folland, T. G.; Fali, A.; White, S. T.; Matson, J. R.; Liu, S.; Aghamiri, N. A.; Edgar, J. H.; Haglund, R. F.; Abate, Y.; Caldwell, J. D. Reconfigurable Infrared Hyperbolic Metasurfaces Using Phase Change Materials. *Nat. Commun.* **2018**, *9*, 4371.
(30) Abedini Dereshgi, S.; Folland, T. G.; Murthy, A. A.; Song, X.; Tanriover, I.; Dravid, V. P.; Caldwell, J. D.; Aydin, K. Lithography-Free IR Polarization Converters via Orthogonal In-Plane Phonons in α-MoO_3 Flakes. *Nat. Commun.* **2020**, *11*, 5771.

https://doi.org/10.1021/acsami.1c12320
ACS Appl. Mater. Interfaces 2021, 13, 48981−48987

(31) Ma, W.; Alonso-González, P.; Li, S.; Nikitin, A. Y.; Yuan, J.; Martín-Sánchez, J.; Taboada-Gutiérrez, J.; Amenabar, I.; Li, P.; Vélez, S.; Tollan, C.; Dai, Z.; Zhang, Y.; Sriram, S.; Kalantar-Zadeh, K.; Lee, S.-T.; Hillenbrand, R.; Bao, Q. In-Plane Anisotropic and Ultra-Low-Loss Polaritons in a Natural Van Der Waals Crystal. *Nature* **2018**, *562*, 557−562.
(32) Zheng, Z.; Chen, J.; Wang, Y.; Wang, X.; Chen, X.; Liu, P.; Xu, J.; Xie, W.; Chen, H.; Deng, S.; Xu, N. Highly Confined and Tunable Hyperbolic Phonon Polaritons in Van Der Waals Semiconducting Transition Metal Oxides. *Adv. Mater.* **2018**, *30*, 1705318.
(33) Zheng, Z.; Xu, N.; Oscurato, S. L.; Tamagnone, M.; Sun, F.; Jiang, Y.; Ke, Y.; Chen, J.; Huang, W.; Wilson, W. L.; Ambrosio, A.; Deng, S.; Chen, H. A Mid-Infrared Biaxial Hyperbolic Van Der Waals Crystal. *Sci. Adv.* **2019**, *5*, No. eaav8690.
(34) Álvarez-Pérez, G.; Folland, T. G.; Errea, I.; Taboada-Gutiérrez, J.; Duan, J.; Martín-Sánchez, J.; Tresguerres-Mata, A. I.; Matson, J. R.; Bylinkin, A.; He, M.; Ma, W. Infrared Permittivity of the Biaxial Van Der Waals Semiconductor α-MoO_3 From Near-and Far-Field Correlative Studies. *Adv. Mater.* **2020**, *32*, 1908176.
(35) Deng, G.; Dereshgi, S. A.; Song, X.; Wei, C.; Aydin, K. Phonon-Polariton Assisted Broadband Resonant Absorption in Anisotropic α-phase MoO_3 Nanostructures. *Phys. Rev. B: Condens. Matter Mater. Phys.* **2020**, *102*, 035408.
(36) Wei, C.; Abedini Dereshgi, S.; Song, X.; Murthy, A.; Dravid, V. P.; Cao, T.; Aydin, K. Polarization Reflector/Color Filter at Visible Frequencies via Anisotropic α-MoO_3. *Adv. Opt. Mater.* **2020**, *8*, 2000088.
(37) Folland, T. G.; Caldwell, J. D. Precise Control of Infrared Polarization Using Crystal Vibrations. *Nature* **2018**, *562*, 499−501.
(38) Zhao, B.; Hu, M.; Ao, X.; Chen, N.; Pei, G. Radiative cooling: A Review of Fundamentals, Materials, Applications, and Prospects. *Appl. Energy* **2019**, *236*, 489−513.
(39) Lee, N.; Kim, T.; Lim, J.-S.; Chang, I.; Cho, H. H. Metamaterial-Selective Emitter for Maximizing Infrared Camouflage Performance with Energy Dissipation. *ACS Appl. Mater. Interfaces* **2019**, *11*, 21250−21257.
(40) Raman, A. P.; Anoma, M. A.; Zhu, L.; Rephaeli, E.; Fan, S. Passive Radiative Cooling Below Ambient Air Temperature under Direct Sunlight. *Nature* **2014**, *515*, 540−544.
(41) Khalichi, B.; Ghobadi, A.; Osgouei, A. K.; Kocer, H.; Ozbay, E. A Transparent All-Dielectric Multifunctional Nanoantenna Emitter Compatible with Thermal Infrared and Cooling Scenarios. *IEEE Access* **2021**, *9*, 98590−98602.
(42) Hossain, M. M.; Gu, M. Radiative Cooling: Principles, Progress, and Potentials. *Adv. Sci.* **2016**, *3*, 1500360.
(43) Hong, S.; Shin, S.; Chen, R. An Adaptive and Wearable Thermal Camouflage Device. *Adv. Funct. Mater.* **2020**, *30*, 1909788.
(44) Buhara, E.; Ghobadi, A.; Khalichi, B.; Kocer, H.; Ozbay, E. Mid-Infrared Adaptive Thermal Camouflage Using a Phase-Change Material Coupled Dielectric Nanoantenna. *J. Phys. D Appl. Phys.* **2021**, *54*, 265105.
(45) Larciprete, M. C.; Centini, M.; Li Voti, R.; Sibilia, C. Selective and Tunable Thermal Emission in Metamaterials Composed of Oriented Polar Inclusions. *J. Opt. Soc. Am. B* **2017**, *34*, 1459−1464.
(46) Larciprete, M. C.; Centini, M.; Paoloni, S.; Dereshgi, S. A.; Tang, K.; Wu, J.; Aydin, K. Effect of Heating/Cooling Dynamics in the Hysteresis Loop and Tunable IR Emissivity of VO_2 Thin Films. *Opt. Express* **2020**, *28*, 39203−39215.
(47) Wan, C.; Zhang, Z.; Woolf, D.; Hessel, C. M.; Rensberg, J.; Hensley, J. M.; Xiao, Y.; Shahsafi, A.; Salman, J.; Richter, S.; Sun, Y.; Qazilbash, M. M.; Schmidt-Grund, R.; Ronning, C.; Ramanathan, S.; Kats, M. A. On the Optical Properties of Thin-Film Vanadium Dioxide from the Visible to the Far Infrared. *Ann. Phys.* **2019**, *531*, 1900188.
(48) Kakiuchida, H.; Jin, P.; Nakao, S.; Tazawa, M. Optical Properties of Vanadium Dioxide Film During Semiconductive−Metallic Phase Transition. *Jpn. J. Appl. Phys.* **2007**, *46*, L113.
(49) Passler, N. C.; Paarmann, A. Generalized 4× 4 Matrix Formalism for Light Propagation in Anisotropic Stratified Media: Study of Surface Phonon Polaritons in Polar Dielectric Heterostructures. *J. Opt. Soc. Am. B* **2017**, *34*, 2128−2139.
(50) Jang, A.-R.; Yoon, J.; Son, S.-B.; Ryu, H. I.; Cho, J.; Shin, K.-H.; Sohn, J. I.; Hong, W.-K. Phase Transition-Induced Temperature-Dependent Phonon Shifts in Molybdenum Disulfide Monolayers Interfaced with a Vanadium Dioxide Film. *ACS Appl. Mater. Interfaces* **2021**, *13*, 3426−3434.
(51) Dereshgi, S. A.; Okyay, A. K. Large Area Compatible Broadband Superabsorber Surfaces in the VIS-NIR Spectrum Utilizing Metal-Insulator-Metal Stack and Plasmonic Nanoparticles. *Opt. Express* **2016**, *24*, 17644−17653.
(52) Abedini Dereshgi, S.; Sisman, Z.; Topalli, K.; Okyay, A. K. Plasmonically Enhanced Metal−Insulator Multistacked Photodetectors with Separate Absorption and Collection Junctions for Near-Infrared Applications. *Sci. Rep.* **2017**, *7*, 42349.
(53) Ghobadi, A.; Dereshgi, S. A.; Hajian, H.; Bozok, B.; Butun, B.; Ozbay, E. Ultra-Broadband, Wide Angle Absorber Utilizing Metal Insulator Multilayers Stack with a Multi-Thickness Metal Surface Texture. *Sci. Rep.* **2017**, *7*, 4755.

https://doi.org/10.1021/acsami.1c12320
ACS Appl. Mater. Interfaces 2021, 13, 48981−48987